

Interpretation-Oriented Cloud Removal via Observation-Anchored Residual Flow with Geo-Contextual Alignment

Ziyao Wang^{1,*}, Maonan Wang^{1,2}, Yucheng He¹, Xianping Ma^{3,†},
Ziyi Wang¹, Hongyang Zhang¹, Yirong Cheng², and Man-on Pun^{1,†}

¹ School of Science and Engineering, The Chinese University of Hong Kong,
Shenzhen, Shenzhen, China

² Shanghai Ai Lab, Shanghai, China

³ Faculty of Geosciences and Engineering, Southwest Jiaotong University, Chengdu,
China

Abstract. Cloud removal (CR) is essential for optical remote sensing, serving as a prerequisite for reliable downstream interpretation, such as semantic segmentation and change detection. However, existing CR approaches often prioritize visual realism while overlooking their impact on subsequent analytical tasks, leading to semantic drift and degraded downstream performance. To address this issue, we propose Geo-Anchored Cloud Removal (GACR), a unified framework that jointly ensures faithful reconstruction and robust interpretability. At its core, GACR incorporates Observation-Anchored Residual Flow (OAR-Flow), which reformulates CR as a physically grounded residual inversion process. By anchoring the generative trajectory to the cloudy observation rather than pure noise, OAR-Flow enables fast, stable, and faithful reconstruction. To further preserve semantic structures critical for downstream interpretation, GACR integrates Geo-Contextual Prior Alignment (GCPA) to constrain the reconstruction within a semantic manifold induced by a Vision Foundation Model (VFM). Consequently, GACR strictly maintains the spatial-semantic integrity of complex landscapes. Extensive experiments across six CR datasets and twelve downstream tasks demonstrate that GACR produces superior reconstruction quality while consistently improving downstream task accuracy. The code is available at <https://github.com/wzy6055/GACR>.

Keywords: Cloud Removal · Remote Sensing · Observation-Anchored Generative Modeling · Geo-Contextual Semantic Alignment

1 Introduction

Optical satellite imagery constitutes a primary data source for a broad spectrum of Earth observation applications, including urban development monitoring, resource management, and land-cover mapping [3, 17, 52, 53]. The reliability of these

* First author. † Co-corresponding authors.

applications fundamentally depends on accurate surface representation and semantic consistency in the observed imagery. However, the presence of clouds severely limits the usability of optical imagery by obscuring surface information and introducing uncertainty in analyses [24, 27]. As a result, cloud removal (CR) has evolved from a simple preprocessing operation to a critical component in the remote sensing interpretation pipeline, motivating extensive efforts toward generating cloud-free and semantically reliable imagery [10, 24].

Recent advances in deep learning-based CR methods can be broadly categorized into denoising-based [36, 50, 51] and generative-based approaches [31, 35, 46, 55]. Denoising-based methods typically treat cloud occlusion as additive residual noise and learn a direct mapping to the underlying clear image. However, these methods are built upon the assumption that the residual noise follows a Gaussian prior distribution [48]. Under heavy occlusion, where surface information is largely obscured rather than merely perturbed, such assumptions often lead to structural ambiguity and over-smoothed reconstructions. In contrast, generative approaches, particularly diffusion-based models, demonstrate a strong capability in synthesizing visually plausible textures under severe cloud coverage. Yet, their inherent stochastic sampling process lacks explicit observation anchoring, frequently resulting in geographically inconsistent structures or semantic drift in heavily occluded regions. While visually realistic, such hallucinated details may contradict the true land-cover distribution, thereby undermining reliability in downstream interpretation tasks.

Beyond the lack of observation anchoring in generative modeling, a more fundamental challenge lies in the visual-fidelity-oriented optimization paradigm underlying most existing CR methods. Current approaches primarily minimize pixel-level discrepancies against cloud-free references, implicitly equating visual fidelity with semantic correctness. Such objectives encourage aggressive artifact removal to maximize conventional image quality metrics (e.g., PSNR, SSIM) [6, 48], yet provide no explicit constraint on preserving task-relevant structural and categorical information. As a result, reconstructed regions may appear visually plausible while deviating from the true geographical context, leading to subtle but critical semantic inconsistencies. When deployed in downstream applications, such as semantic segmentation, these inconsistencies accumulate and translate into degraded representational reliability. This misalignment between low-level restoration objectives and high-level interpretative requirements limits the practical utility of current CR methods.

To address these challenges, we propose Geo-Anchored Cloud Removal (GACR), a unified framework built upon Observation-Anchored Residual Flow (OAR-Flow). Instead of initiating generation from pure noise, OAR-Flow starts from the cloudy observation and models CR as a physically grounded residual inversion process. By initializing the generative trajectory with structured perturbations around the observed image, the model adapts its behavior according to cloud opacity. In thin-cloud regions, where surface signals remain partially observable, the observation dominates the dynamics, guiding the model to perform physical inversion and preserve subtle yet authentic surface cues. In contrast,

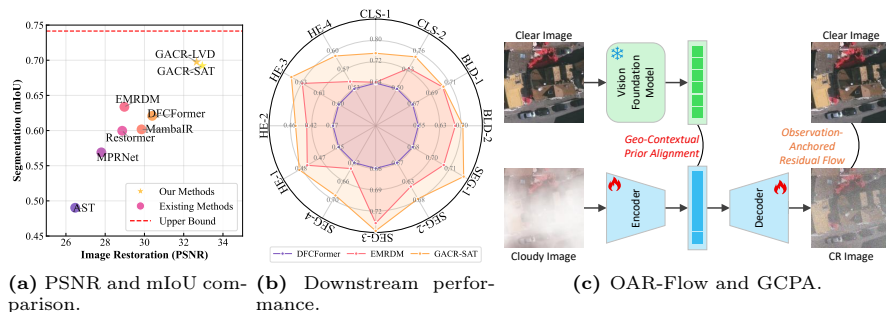


Fig. 1: (a) Comparison with existing methods in terms of PSNR and mIoU on Vaihingen-CR-Thick. (b) Performance across 12 downstream tasks, where the outermost ring denotes the upper bound. (c) GACR reconstructs cloud-free imagery from cloudy observations via OAR-Flow, while GCPA constrains the generative process within a geo-contextually consistent semantic manifold.

under thick cloud coverage where information is largely obscured, residual perturbations provide generative flexibility, enabling controlled semantic completion. This observation-anchored mechanism shortens the generative trajectory and suppresses unnecessary stochastic exploration, ensuring that reconstructed structures remain spatially aligned with the original observation while avoiding geographically implausible artifacts.

While physical anchoring stabilizes the generative dynamics, visual fidelity alone remains insufficient to guarantee semantic reliability for downstream interpretation. To bridge the gap between low-level restoration and high-level semantic preservation, we introduce Geo-Contextual Prior Alignment (GCPA), which leverages representational priors from a pretrained Vision Foundation Model (VFM) to guide cloud removal. Rather than optimizing solely for pixel-level similarity, GCPA aligns dense representations within a VFM-induced semantic manifold, encouraging reconstructed regions to remain coherent with their surrounding geographical context. This alignment is enforced through the proposed Geo-Contextual Integrity Loss (GCI Loss), which explicitly regularizes the generative process to preserve task-relevant structural patterns and category-specific semantic signatures. By jointly integrating OAR-Flow and GCPA, our framework produces cloud-free reconstructions that maintain both visual fidelity and semantic integrity. Extensive experiments across six CR datasets and twelve downstream tasks demonstrate that GACR consistently improves both reconstruction quality and downstream interpretation accuracy, with PSNR gains reaching 3.3 dB, semantic segmentation improvements of 3.1 mIoU, and approximately $5\times$ faster convergence, effectively mitigating semantic distortion, as shown in Fig. 1.

The main contributions of this work are:

- We formulate cloud removal as an interpretation-oriented generative inversion problem and propose OAR-Flow, which grounds generation in the observed cloudy image to achieve stable and faithful reconstruction.
- We introduce GCPA, which constrains reconstruction within a semantic manifold induced by a VFM to preserve task-relevant structural patterns and category-specific information.
- Extensive experiments across six benchmarks and twelve downstream tasks demonstrate that GACR consistently improves reconstruction quality while yielding higher accuracy in downstream interpretation tasks.

2 Related Work

2.1 Cloud Removal Method

CR is a fundamental preprocessing step in Earth observation, aiming to recover cloud-free imagery for reliable surface analysis. With deep learning, data-driven CR methods have greatly improved visual quality and adaptability, and can be broadly grouped into residual-prediction-based and generation-based methods. The former estimates cloud residuals or clean reflectance using CNNs [26, 54], Transformers [22, 48], or Mamba architectures [15, 16, 29, 38]. However, they commonly rely on the cloud-as-residual assumption, which oversimplifies complex atmospheric scattering and limits recovery in regions severely occluded by thick clouds. Generation-based models instead synthesize cloud-free images through adversarial or diffusion mechanisms. Early GAN-based methods [5, 11, 14, 35, 43] improved perceptual realism but often suffered from instability and artifacts, whereas recent diffusion-based approaches [31, 41, 46, 55] achieve better fidelity and convergence. Nevertheless, most CR models are still mainly optimized for pixel-level similarity, offering limited semantic constraints for downstream interpretation tasks [6, 48]. In contrast, our framework introduces OAR-Flow and GCPA to jointly promote physically grounded reconstruction and semantic integrity.

2.2 Diffusion and Flow Model

Diffusion models have recently shown remarkable success in image generation [12, 21, 47, 49], evolving from DDPM [19, 37] and DDIM [44] to score-based SDE/ODE formulations [23, 45]. Through iterative denoising of Gaussian noise, they achieve higher fidelity and diversity than GAN-based [13] and VAE-based [25] paradigms. Early studies mainly used U-Net architectures [46, 55], while recent Diffusion Transformers (DiT) [39] improve scalability. However, many transformer-based diffusion models work in latent space [34, 39, 40], which limits pixel-level restoration. HDiT [7] therefore enables direct pixel-space reconstruction, with MRDM [33] and EMRDM [31] further adapting diffusion to CR scenarios. Nevertheless, diffusion models often require long stochastic sampling trajectories and high computational cost [19]. Flow matching methods [1, 2, 28, 30]

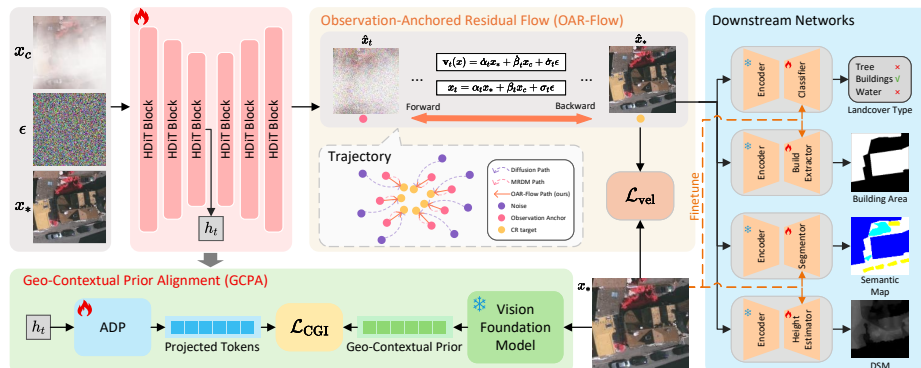


Fig. 2: Overview of the proposed GACR framework. (1) OAR-Flow reconstructs cloud-free imagery from cloudy observations via an observation-anchored residual trajectory, replacing pure noise initialization with a physically grounded anchor and enabling stable deterministic flow dynamics supervised by \mathcal{L}_{vel} . (2) GCPA leverages a pretrained Vision Foundation Model to extract geo-contextual representations from clean images, enforcing semantic consistency through the \mathcal{L}_{GCI} and constraining the generative process within a coherent feature manifold. (3) Downstream networks trained on cloud-free data are used to evaluate the semantic fidelity and interpretation reliability of the reconstructed CR outputs.

reformulate diffusion as deterministic probability flow ODEs for more efficient trajectory learning. Different from existing flow-based CR methods, OAR-Flow introduces an observation-conditioned residual formulation that grounds generative dynamics in the cloudy input rather than unconditional noise.

3 Methodology

This section presents the proposed GACR framework illustrated in Fig. 2. We start by reviewing the theoretical background in Sec. 3.1. We then introduce OAR-Flow in Sec. 3.2, followed by GCPA in Sec. 3.3. Finally, we describe the downstream evaluation protocols in Sec. 3.4.

3.1 Preliminaries

A diffusion process with an initial distribution $p_0(x)$ can be described by the following stochastic differential equation (SDE) [9, 32, 45] for $t \in [0, T]$:

$$dx = f(x, t) dt + g(t) d\mathbf{w}, \quad x(0) \sim p_0(x), \quad (1)$$

where $f(\cdot, \cdot)$ and $g(\cdot)$ denote the drift and diffusion coefficients, and \mathbf{w} is a standard Wiener process. The corresponding reverse-time SDE is given by:

$$dx = [f(x, t) - g(t)^2 \nabla_x \log p_t(x)] dt + g(t) d\hat{\mathbf{w}}, \quad (2)$$

where $\hat{\mathbf{w}}$ is the reverse-time Wiener process and $\nabla_x \log p_t(x)$ denotes the score function of the marginal distribution $p_t(x)$. In image restoration problems, the objective is to model the conditional distribution between degraded and clean images by constructing a continuous trajectory that links the two states.

To better characterize structured degradation, several works introduced modified diffusion dynamics that interpolate between a reference state and the target distribution via mean-reverting formulations [31, 33]. A representative forward process can be written as

$$dx = \theta_t(\mu - x) dt + \sigma_t d\mathbf{w}, \quad (3)$$

where μ denotes a reference state and θ_t, σ_t control the drift strength and stochastic noise intensity, respectively. This formulation provides an interpretable trajectory that gradually transports samples toward a designated state, offering a structured alternative to purely noise-driven diffusion. The corresponding reverse process can be expressed in either SDE or ODE form depending on the parameterization [31, 33]. Such formulations provide a flexible basis for designing conditional generative dynamics, which we further specialize for CR in the following section.

3.2 Observation-Anchored Residual Flow

Forward Process. Unlike unconditional generation, CR aims to recover the clean surface image x_* from a structured degradation x_c (cloudy observation). In remote sensing imagery, cloud coverage is not random noise but a spatially varying atmospheric scattering layer that partially or fully obscures surface reflectance. To explicitly model this conditional relationship, OAR-Flow constructs a continuous trajectory that transports samples between the clean state x_* and the cloudy observation x_c under structured perturbation, as illustrated in Fig. 2.

We define the forward interpolant as:

$$x_t = \alpha_t x_* + \beta_t x_c + \sigma_t \epsilon, \quad (4)$$

where $\epsilon \sim \mathcal{N}(0, I)$ denotes Gaussian noise, and α_t, β_t , and σ_t are time-dependent coefficients satisfying:

$$\begin{aligned} \alpha_0 &= 1, & \beta_0 &= 0, & \sigma_0 &= 0, \\ \alpha_T &= 0, & \beta_T &> 0. \end{aligned} \quad (5)$$

Here, x_c acts as an observation anchor. In thin-cloud regions, where surface signals remain partially observable, the contribution of x_c preserves low-frequency and structural cues. In thick-cloud regions, the stochastic component ϵ provides generative flexibility for semantic completion. This formulation explicitly reflects the opacity-aware characteristics of cloud degradation.

In practice, we adopt a simple linear schedule:

$$\alpha_t = 1 - t, \quad \beta_t = \rho t, \quad \sigma_t = t, \quad (6)$$

where ρ controls the strength of the observation anchor relative to stochastic perturbations, ensuring that the trajectory remains grounded in the cloudy observation while retaining flexibility in severely occluded regions.

Backward Process. The marginal distribution $p_t(x)$ induced by Eq. (4) satisfies the transport equation [1, 34]:

$$\partial_t p_t(x) + \nabla_x \cdot (\mathbf{v}_t(x)p_t(x)) = 0, \quad (7)$$

where $\mathbf{v}_t(x)$ denotes the velocity field of the deterministic probability flow.

Following the flow matching formulation, the ideal velocity field can be expressed as:

$$v_t(x) = \mathbb{E}[\dot{\alpha}_t x_* + \dot{\beta}_t x_c + \dot{\sigma}_t \epsilon \mid x_t = x], \quad (8)$$

which explicitly decomposes the dynamics into three components: clean target guidance, observation anchoring, and stochastic perturbation. This residual decomposition differs from purely noise-driven flows by incorporating structured observational information into the trajectory. The correspondence between the marginal distribution $p_t(x)$ and the velocity formulation in Eq. (8) follows from the transport equation in Eq. (7), and the detailed derivation is provided in Appendix A.

We parameterize the velocity field using a neural network \mathbf{u}_t :

$$\mathbf{u}_t(x) = \text{Net}_\theta(x_t, t, x_c), \quad (9)$$

where x_c is provided as a condition to preserve spatial alignment with the observed cloudy image.

During inference, the clean estimate is obtained by integrating the deterministic flow from $t = T$ to $t = 0$:

$$\hat{x}_{t-1} = \hat{x}_t + \Delta t \mathbf{u}_t(\hat{x}_t), \quad (10)$$

yielding the final reconstruction $\hat{x}_* = \hat{x}_0$. Because the trajectory remains anchored to x_c throughout integration, the reconstructed surface structures are spatially consistent with the original observation, effectively reducing geographically implausible artifacts.

3.3 Geo-Contextual Prior Alignment

To jointly ensure reconstruction fidelity and semantic integrity in CR, we optimize OAR-Flow under two complementary objectives: a velocity matching loss \mathcal{L}_{vel} in pixel space and a geo-contextual consistency constraint loss \mathcal{L}_{GCI} in the representation space.

Velocity Matching Loss. The primary supervision for OAR-Flow is to match the analytical velocity defined in Eq. (8). The network \mathbf{u}_t is trained to approximate the target velocity field:

$$\begin{aligned} \mathcal{L}_{\text{vel}} &= \mathbb{E} \left[\left\| \mathbf{u}_t(x_t) - \mathbf{v}_t(x_t) \right\|^2 \right] \\ &= \mathbb{E}_{x_*, \epsilon, x_c} \left[\left\| \mathbf{u}_t(x_t) - \dot{\alpha}_t x_* - \dot{\beta}_t x_c - \dot{\sigma}_t \epsilon \right\|^2 \right]. \end{aligned} \quad (11)$$

This objective ensures that the learned flow follows the observation-anchored residual trajectory defined in OAR-Flow. The network is implemented using an HDiT-based backbone [7], receiving the current state x_t , timestep t , and the cloudy observation x_c as condition, and predicting the deterministic velocity toward the clean state.

Geo-Contextual Integrity Loss. While velocity supervision guarantees pixel-level reconstruction consistency, it does not explicitly enforce preservation of land-cover semantics. In remote sensing imagery, geographical context exhibits strong structural continuity (e.g., forests form contiguous regions and urban layouts follow spatial regularity). To maintain such geo-contextual coherence, we introduce GCPA, implemented through the proposed GCI Loss.

Let $f_{\text{vfm}}(\cdot)$ denote a pretrained VFM encoder. The geo-contextual prior of the clear image is defined as

$$z_* = f_{\text{vfm}}(x_*) \in \mathbb{R}^{B \times L \times D}. \quad (12)$$

We extract the intermediate feature $h_t \in \mathbb{R}^{B \times C \times H \times W}$ from the bottleneck of the HDiT backbone and map it into the same representation space via an Adaptive Projector (ADP):

$$\begin{aligned} z_t &= \text{ADP}(h_t) \\ &= \text{MLP}(\text{RE}(\text{AP}(h_t))), \end{aligned} \quad (13)$$

where $\text{RE}(\cdot)$ and $\text{AP}(\cdot)$ denote rearrangement and adaptive pooling operations, respectively.

The GCI Loss is defined as a patch-wise cosine similarity:

$$\mathcal{L}_{\text{GCI}} = -\mathbb{E} \left[\frac{1}{N} \sum_{n=1}^N \frac{\langle z_*^{[n]}, z_t^{[n]} \rangle}{\|z_*^{[n]}\|_2 \|z_t^{[n]}\|_2} \right], \quad (14)$$

where n indexes spatial tokens. By aligning reconstructed features with the VFM-induced semantic manifold, this loss constrains the generative process to remain consistent with large-scale geographical structures, thereby reducing semantic drift in heavily occluded regions.

Unified Objective. The overall training objective is:

$$\mathcal{L} = \mathcal{L}_{\text{vel}} + \lambda \mathcal{L}_{\text{GCI}}, \quad (15)$$

where λ balances reconstruction fidelity and geo-contextual integrity. Ablation analysis of the objective components is provided in Section 4.4.

3.4 Downstream Networks

We evaluate GACR on four remote sensing tasks: land-cover classification, building extraction, semantic segmentation, and height estimation as shown in Fig. 2. These tasks assess whether reconstructed CR results preserve task-relevant semantic and structural information.

We adopt a pretrained DINOv3 backbone [42] as a unified visual encoder for downstream evaluation. For each task, the backbone is frozen and paired with a lightweight decoder trained on clear images to establish reliable reference performance. Notably, the VFM used for GCPA and the downstream encoders are independent, ensuring that downstream evaluation does not share parameters or supervision signals with the upstream semantic guidance. The architectural details of the downstream networks are presented in Appendix B.

4 Experiments and Discussion

4.1 Implementation Details

Dataset. To enable a unified evaluation of both reconstruction fidelity and downstream performance, we construct a comprehensive benchmark for joint assessment. Specifically, we employ six CR datasets, including two publicly available datasets: CUHKCR-EXT-GZ and CUHKCR-EXT-CS [48], along with four synthetic cloud datasets constructed by ourselves: Potsdam-CR-thin, Potsdam-CR-thick, Vaihingen-CR-thin, and Vaihingen-CR-thick. These datasets cover both real and simulated cloud scenarios, encompassing thin and thick cloud conditions to reflect varying levels of opacity and structural occlusion.

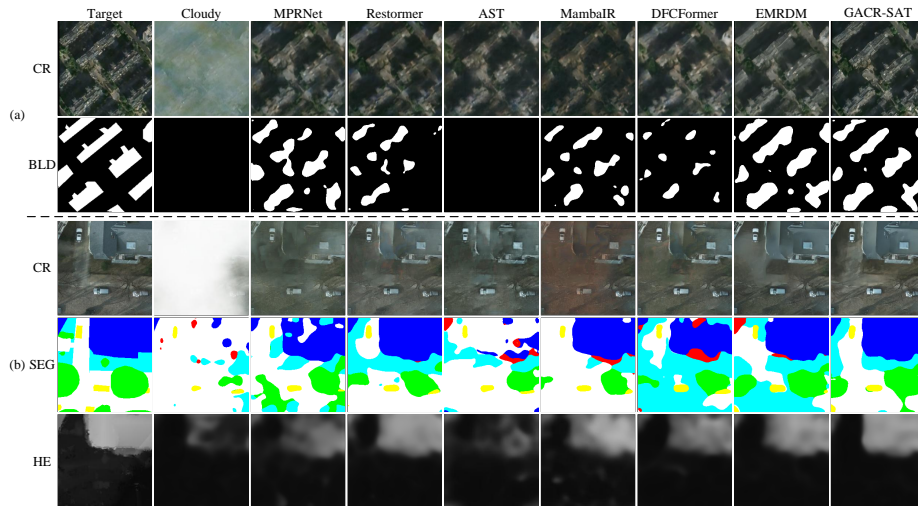
Downstream Tasks. CUHKCR-EXT-GZ and CUHKCR-EXT-CS support land-cover classification (CLS-1 and CLS-2) and building extraction (BLD-1 and BLD-2), while the four synthetic datasets include semantic segmentation (SEG-1 to SEG-4) and height estimation (HE-1 to HE-4). These tasks evaluate whether reconstructed CR outputs preserve task-relevant semantic structures and spatial consistency. Further details on dataset construction and the cloud synthesis process are provided in Appendix C.

Model Settings. For GCPA, we employ two pretrained DINOv3 variants as the VFM module: ViT-L/16-SAT-300M and ViT-L/16-LVD-1689M. Model configurations are denoted as GACR-SAT/p or GACR-LVD/p, where ‘‘SAT’’ and ‘‘LVD’’ indicate the corresponding VFM pretraining variants, and ‘‘/p’’ specifies the patch size used in OAR-Flow. In our experiments, the upstream VFM for geo-contextual guidance and the downstream encoder for evaluation are initialized from different pretrained weights, ensuring no parameter sharing between guidance and evaluation stages. This separation avoids potential bias arising from shared representation priors and enables a fair assessment of downstream improvements. To further verify robustness with respect to backbone selection, we additionally conduct experiments using heterogeneous downstream encoders, with detailed results reported in Appendix D.

Evaluation Metrics. For CR evaluation, we adopt PSNR and SSIM to measure reconstruction fidelity from complementary perspectives of distortion, perceptual similarity, and error magnitude. For downstream evaluation, we report accuracy (Acc.) for CLS, IoU for BLD, mIoU for SEG, and RMSE for HE. More implementation details of metrics and training settings are provided in Appendix D.

Table 1: Quantitative comparison across six CR datasets. The best and second-best scores are marked in **bold** and underline, respectively.

Model	CUHKCR-EXT-GZ		CUHKCR-EXT-CS		Potsdam-CR-thin		Potsdam-CR-thick		Vaihingen-CR-thin		Vaihingen-CR-thick	
	PSNR \uparrow	SSIM \uparrow	PSNR \uparrow	SSIM \uparrow	PSNR \uparrow	SSIM \uparrow	PSNR \uparrow	SSIM \uparrow	PSNR \uparrow	SSIM \uparrow	PSNR \uparrow	SSIM \uparrow
MPRNet [36]	23.454	0.712	23.365	0.695	28.349	0.960	26.418	0.902	31.209	0.978	27.805	0.935
Restormer [50]	25.839	0.743	23.632	0.710	31.413	0.970	28.831	0.922	31.210	0.970	28.867	0.922
AST [51]	25.482	0.735	23.365	0.695	28.924	0.957	25.886	0.890	29.877	0.973	26.471	0.916
MambaIR [16]	25.626	0.733	23.445	0.704	30.881	0.967	27.027	0.903	32.764	0.983	29.852	0.945
DFCFormer [48]	25.816	<u>0.746</u>	23.876	0.711	30.836	0.969	28.196	0.917	33.342	0.985	30.396	0.951
EMRDM [31]	25.862	0.747	23.736	0.712	30.335	0.972	27.199	0.923	33.620	0.988	28.979	0.951
GACR-SAT/2	25.964	0.736	24.230	0.709	33.141	0.975	30.578	0.934	36.293	0.990	33.018	0.964
GACR-LVD/2	25.899	0.735	24.220	0.707	32.880	0.975	30.308	0.932	35.749	0.989	32.656	0.963
GACR-SAT/1	26.100	0.744	24.354	<u>0.713</u>	33.642	0.976	31.049	0.938	36.918	0.991	34.048	0.970
GACR-LVD/1	<u>26.059</u>	0.744	<u>24.331</u>	0.714	<u>33.305</u>	<u>0.975</u>	<u>30.586</u>	<u>0.935</u>	<u>36.590</u>	<u>0.991</u>	<u>33.808</u>	<u>0.969</u>

**Fig. 3:** Visualization of CR and downstream results. (a) The CR results on CUHKCR-EXT-GZ and the corresponding BLD results. (b) The CR results on Potsdam-CR-thick and the corresponding SEG and HE results.

4.2 CR Evaluation

This section evaluates the reconstruction fidelity of CR results. Quantitative comparisons are reported in Tab. 1. On the CUHKCR-EXT datasets, GACR achieves highly competitive performance across most metrics. Except for a slightly lower SSIM on CUHKCR-EXT-GZ, GACR consistently surpasses existing approaches in terms of PSNR and RMSE, indicating a favorable balance between pixel-level accuracy and perceptual consistency. For example, on CUHKCR-EXT-CS, GACR-SAT/1 achieves a PSNR of 24.354, improving upon the strongest baseline by approximately 0.5 dB. Notably, the improvements are not limited to a single metric but are consistently reflected across multiple evaluation metrics, demonstrating the robustness of the proposed reconstruction strategy.

Table 2: Quantitative comparison of different tasks on downstream networks with ViT-L/16-LVD-1689M weight, including classification (CLS), building extraction (BLD), semantic segmentation (SEG), and height estimation (HE). The best and second-best results are highlighted in **bold** and underline, respectively.

Model	CLS-1	CLS-2	BLD-1	BLD-2	SEG-1	SEG-2	SEG-3	SEG-4	HE-1	HE-2	HE-3	HE-4
	Acc. \uparrow	Acc. \uparrow	IoU \uparrow	IoU \uparrow	mIoU \uparrow	mIoU \uparrow	mIoU \uparrow	mIoU \uparrow	RMSE \downarrow	RMSE \downarrow	RMSE \downarrow	RMSE \downarrow
Upper Bound	0.882	0.916	0.718	0.762	0.733	0.733	0.755	0.755	1.868	1.868	1.477	1.477
Lower Bound	0.746	0.739	0.669	0.596	0.657	0.490	0.677	0.550	2.144	2.703	1.672	2.095
End-to-End	0.833	0.876	0.691	0.698	0.709	0.643	0.737	0.684	2.000	2.245	1.583	1.830
MPRNet [36]	0.809	0.752	0.653	0.654	0.707	0.615	0.741	0.671	1.987	2.412	1.549	1.757
Restormer [50]	0.803	0.744	0.655	0.660	0.710	0.650	0.718	0.675	1.913	2.228	1.520	1.681
AST [51]	<u>0.813</u>	0.767	0.668	0.651	0.697	0.580	0.736	0.632	2.019	2.492	1.585	1.885
MambaIR [16]	0.759	<u>0.778</u>	0.660	0.648	0.713	0.620	0.736	0.671	1.948	2.350	1.552	1.697
DFCFormer [48]	0.763	0.771	0.659	0.657	0.713	0.630	0.722	0.671	1.948	2.317	1.526	1.687
EMRDM [31]	0.776	0.726	<u>0.703</u>	0.696	0.722	0.668	0.747	0.692	1.902	2.133	1.512	1.629
GACR-SAT/2	0.833	0.781	0.704	0.710	0.727	0.699	0.750	0.737	<u>1.891</u>	2.014	1.482	1.554
GACR-LVD/2	0.806	0.768	0.702	<u>0.704</u>	<u>0.727</u>	<u>0.695</u>	<u>0.748</u>	<u>0.728</u>	1.889	<u>2.025</u>	<u>1.490</u>	<u>1.575</u>

On the four synthetic datasets, GACR demonstrates clear advantages under both thin- and thick-cloud conditions. In thin-cloud scenarios, where surface structures remain partially observable, the observation-anchored formulation effectively preserves fine-grained textures and low-frequency spatial continuity, preventing unnecessary alterations to already reliable regions. This leads to the highest PSNR of 33.642 dB on Potsdam-CR-thin and 36.918 dB on Vaihingen-CR-thin with GACR-SAT/1. In thick-cloud settings, where large areas are severely occluded and lack direct visual cues, the residual generative component provides controlled semantic completion guided by the anchored trajectory. This mechanism enables the model to recover plausible yet geographically consistent structures, resulting in consistent improvements over prior methods across multiple quantitative metrics. The performance gains under heavy occlusion further validate the effectiveness of modeling CR as a physically grounded residual inversion process.

We further evaluate two patch-size configurations to examine the trade-off between reconstruction granularity and computational cost. Results indicate that GACR-SAT/2 already surpasses existing methods by a clear margin, confirming that the proposed framework remains effective even under coarser spatial partitioning. A smaller patch size (GACR-SAT/1) further enhances reconstruction fidelity by enabling finer spatial modeling and more detailed residual refinement. However, considering computational efficiency and fairness in comparison with existing baselines, we adopt $p = 2$ in subsequent experiments unless otherwise specified. Qualitative comparisons are shown in Fig. 3, where GACR produces sharper structural boundaries and fewer texture inconsistencies. Additional visualizations are provided in Appendix E to further illustrate the stability of the reconstruction results across diverse cloud conditions.

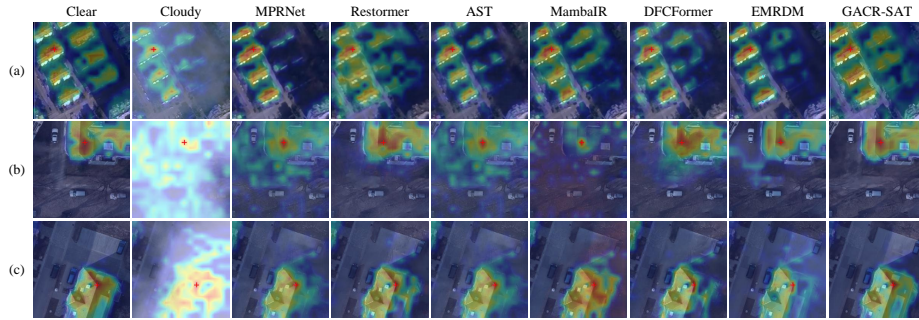


Fig. 4: Heatmaps of different CR obtained from the pretrained DINOv3 ViT-L/16-LVD-1689M. Regions with higher intensity indicate stronger similarity to the locations marked by red crosses.

4.3 Downstream Evaluation

This section evaluates downstream performance to examine whether GACR preserves task-relevant semantic structures beyond pixel-level fidelity. The quantitative results in Tab. 2 are obtained using a DINOv3-based downstream encoder initialized with the ViT-L/16-LVD-1689M weights. In the table, the upper bound denotes testing directly on clear images, the lower bound represents performance without CR preprocessing, and end-to-end refers to training and testing downstream models directly on cloudy images. Results obtained using the ViT-L/16-SAT-300M weights are provided in Appendix E.

Across all downstream tasks, GACR consistently achieves superior downstream performance compared with existing CR methods. In particular, GACR-SAT/2 attains the highest classification accuracies of 0.833 and 0.781 on CLS-1 and CLS-2, exceeding the strongest baseline (AST) by 2.0% and 1.4%, respectively. For height estimation, GACR-SAT/2 achieves the lowest RMSE values of 1.891 and 1.482 on HE-1 and HE-3, outperforming the second-best method by 0.1-0.2. These improvements indicate that GACR better preserves semantic consistency and spatial structure critical for downstream recognition.

For the CLS task, the performance gap between different CR methods is relatively small. We observe that the end-to-end approach yields results close to the upper bound and, in some cases, performs comparably to inputs preprocessed via CR. This phenomenon can be attributed to the global nature of classification, where coarse semantic representations are less sensitive to localized cloud occlusion. The t-SNE analysis in Appendix E further supports this observation: cloudy inputs already form distinguishable clusters similar to cloud-free samples, implying that CR only provides limited additional separability.

In contrast, for dense prediction tasks such as segmentation and height estimation, CR leads to substantial downstream improvements, with GACR consistently delivering greater gains than competing methods. As shown in Fig. 3, different CR approaches enhance land-cover discriminability to varying extents, yet GACR produces more distinct and semantically coherent object boundaries.

To further analyze this behavior, we present feature activation maps in Fig. 4. For example, in row (a), GACR enables clearer separation of cloud-affected buildings on the right side of the image, indicating improved semantic localization. Moreover, Fig. 5 visualizes feature distance distributions across methods. While cloudy inputs exhibit a noticeable distribution shift relative to clear references, GACR more effectively aligns the feature distribution with that of the cloud-free references. This observation is consistent with the geo-contextual alignment mechanism, which constrains reconstruction within a semantically coherent feature manifold.

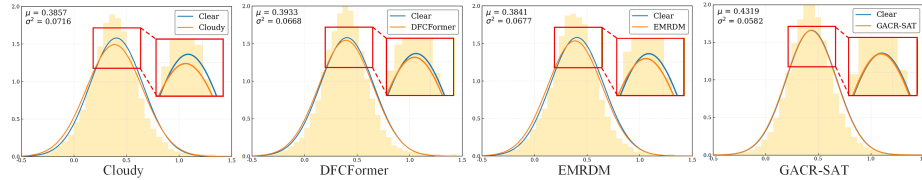


Fig. 5: Feature distance distribution comparison between CR result and corresponding cloud-free reference.

4.4 Ablation Study

Convergence Speed. Fig. 6 presents the PSNR progression over training steps for EMRDM, OAR-Flow without GCPA, and the complete GACR model. Compared with EMRDM, OAR-Flow converges substantially faster, reaching the high-PSNR regime with significantly fewer iterations. Specifically, OAR-Flow achieves a comparable PSNR level using approximately one-third of the training steps required by EMRDM, corresponding to about a $3\times$ acceleration in convergence. This improvement highlights the optimization efficiency introduced by the observation-anchored residual trajectory. Furthermore, incorporating GCPA further accelerates convergence. The complete GACR not only attains higher PSNR but also converges approximately $5\times$ faster than EMRDM.

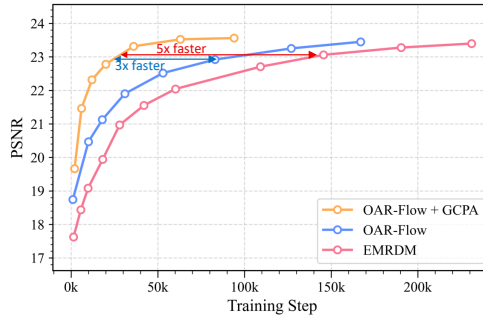


Fig. 6: The introduction of OAR-Flow and GCPA significantly accelerates the convergence of training.

Effectiveness of Model Choice. To investigate the effectiveness of each module, we perform an ablation study on the CUHKCR-EXT-CS dataset, as reported in Tab. 3. Four configurations are compared to disentangle the effects

Table 3: Comparison of different model settings on CUHKCR-EXT-CS.

Method	PSNR \uparrow	SSIM \uparrow	CLS \uparrow	BLD \uparrow	GFLOPs
DiT + MRDM	<u>24.037</u>	0.707	0.670	0.693	697.20
HDiT + MRDM	23.736	0.712	<u>0.726</u>	0.696	166.72
HDiT + OAR-Flow	23.986	0.698	0.690	<u>0.700</u>	56.05
HDiT + OAR-Flow + GCPA	24.230	<u>0.709</u>	0.781	0.710	56.05

of generative formulation and geo-contextual alignment. The diffusion-based baseline corresponding to EMRDM serves as a reference, while the complete GACR represents the final configuration. Although DiT-based modeling produces competitive visual results, it incurs substantially higher computational cost (GFLOPs = 697.20). Replacing diffusion dynamics with OAR-Flow consistently improves reconstruction metrics while maintaining efficiency. Moreover, incorporating GCPA further enhances both CR quality and downstream performance, indicating that geo-contextual alignment effectively mitigates semantic drift and strengthens interpretation reliability.

Effectiveness of λ and patch size p . We further conduct ablation studies on key hyperparameters in Tab. 4, including the balancing coefficient λ for GCI and the patch size p . When $\lambda = 0.5$, the model achieves the best trade-off between reconstruction fidelity and downstream performance. This indicates that moderate regularization enhances semantic consistency without over-constraining pixel-level refinement, whereas overly small or

Table 4: Hyperparameter analysis on Vaihingen-CR-Thick.

	PSNR \uparrow	SSIM \uparrow	SEG \uparrow	HE \downarrow	GFLOPs
λ $p = 2$					
0.2	33.073	0.965	0.728	1.578	-
0.5	33.018	0.964	0.737	1.554	-
1.0	32.838	0.964	0.730	1.563	-
2.0	32.720	0.963	0.729	1.576	-
5.0	32.615	0.962	0.727	1.596	-
p $\lambda = 0.5$					
4	30.303	0.949	0.693	1.616	14.15
2	33.018	0.964	0.737	1.554	56.05
1	33.799	0.969	0.720	1.548	223.60

large λ values degrade either reconstruction quality or downstream metrics. Regarding patch size, smaller values lead to improved visual quality due to finer spatial modeling; however, setting $p = 1$ significantly increases computational cost in terms of FLOPs. Therefore, $p = 2$ is adopted as the default configuration in our experiments to balance reconstruction quality and computational efficiency while maintaining fair comparison with existing methods.

5 Conclusion

In this paper, we present GACR, an interpretation-oriented framework that jointly improves reconstruction fidelity and downstream reliability. With OAR-Flow, CR is reformulated as a physically grounded residual inversion process

anchored to cloudy observations, reducing geographically implausible artifacts. Meanwhile, GCPA constrains reconstruction within a VFM-induced semantic manifold to preserve task-relevant structures and category-specific information. Extensive evaluations on six datasets and twelve downstream tasks show that GACR consistently enhances both reconstruction quality and task accuracy across diverse cloud conditions and remote sensing scenarios. These results suggest that coupling observation-anchored physical priors with semantic constraints enables CR to move beyond visual enhancement toward a reliable, semantics-preserving foundation for Earth observation.

Acknowledgements

This work was supported by the Guangdong Science and Technology Department (Grant No. 2025A0505000062) and the Hong Kong Research Grants Council through the General Research Fund (Grant No. 17617024).

References

1. Albergo, M.S., Boffi, N.M., Vanden-Eijnden, E.: Stochastic interpolants: A unifying framework for flows and diffusions. arXiv preprint arXiv:2303.08797 (2023)
2. Albergo, M.S., Vanden-Eijnden, E.: Building normalizing flows with stochastic interpolants. In: The Eleventh International Conference on Learning Representations (2023)
3. Astruc, G., Gonthier, N., Mallet, C., Landrieu, L.: Omnisat: Self-supervised modality fusion for earth observation. In: European Conference on Computer Vision. pp. 409–427. Springer (2024)
4. Bechtel, B., Demuzere, M., Stewart, I.D.: A weighted accuracy measure for land cover mapping: Comment on johnson et al. local climate zone (LCZ) map accuracy assessments should account for land cover physical characteristics that affect the local thermal environment. *remote sens.* 2019, 11, 2420. *Remote Sensing* **12**(11), 1769 (2020)
5. Bermudez, J.D., Happ, P.N., Oliveira, D.A.B., Feitosa, R.Q.: SAR to optical image synthesis for cloud removal with generative adversarial networks. *ISPRS Annals of the Photogrammetry, Remote Sensing and Spatial Information Sciences* **4**, 5–11 (2018)
6. Chen, I., Chen, W.T., Liu, Y.W., Chiang, Y.C., Kuo, S.Y., Yang, M.H., et al.: Unirestore: Unified perceptual and task-oriented image restoration model using diffusion prior. In: Proceedings of the Computer Vision and Pattern Recognition Conference. pp. 17969–17979 (2025)
7. Crowson, K., Baumann, S.A., Birch, A., Abraham, T.M., Kaplan, D.Z., Shippole, E.: Scalable high-resolution pixel-space image synthesis with hourglass diffusion transformers. In: International Conference on Machine Learning (2024)
8. Czerkawski, M., Atkinson, R., Michie, C., Tachtatzis, C.: Satellitecloudgenerator: controllable cloud and shadow synthesis for multi-spectral optical satellite images. *Remote Sensing* **15**(17), 4138 (2023)
9. De Bortoli, V., Mathieu, E., Hutchinson, M., Thornton, J., Teh, Y.W., Doucet, A.: Riemannian score-based generative modelling. *Advances in neural information processing systems* **35**, 2406–2422 (2022)

10. Ebel, P., Xu, Y., Schmitt, M., Zhu, X.X.: SEN12MS-CR-TS: A remote-sensing data set for multimodal multitemporal cloud removal. *IEEE Transactions on Geoscience and Remote Sensing* **60**, 1–14 (2022)
11. Enomoto, K., Sakurada, K., Wang, W., Fukui, H., Matsuoka, M., Nakamura, R., Kawaguchi, N.: Filmy cloud removal on satellite imagery with multispectral conditional generative adversarial nets. In: *Proceedings of the IEEE conference on computer vision and pattern recognition workshops*. pp. 48–56 (2017)
12. Feng, C., Chen, Z., Holynski, A., Efros, A.A., Owens, A.: GPS as a control signal for image generation. In: *Proceedings of the Computer Vision and Pattern Recognition Conference*. pp. 2766–2778 (2025)
13. Goodfellow, I., Pouget-Abadie, J., Mirza, M., Xu, B., Warde-Farley, D., Ozair, S., Courville, A., Bengio, Y.: Generative adversarial networks. *Communications of the ACM* **63**(11), 139–144 (2020)
14. Grohnfeldt, C., Schmitt, M., Zhu, X.: A conditional generative adversarial network to fuse SAR and multispectral optical data for cloud removal from Sentinel-2 images. In: *IGARSS 2018-2018 IEEE International Geoscience and Remote Sensing Symposium*. pp. 1726–1729. IEEE (2018)
15. Gu, Y., Meng, Y., Ji, J., Sun, X.: ACL: Activating capability of linear attention for image restoration. In: *Proceedings of the Computer Vision and Pattern Recognition Conference*. pp. 17913–17923 (2025)
16. Guo, H., Li, J., Dai, T., Ouyang, Z., Ren, X., Xia, S.T.: MambaIR: A simple baseline for image restoration with state-space model. In: *European Conference on Computer Vision*. pp. 222–241. Springer (2024)
17. Guo, X., Lao, J., Dang, B., Zhang, Y., Yu, L., Ru, L., Zhong, L., Huang, Z., Wu, K., Hu, D., et al.: Skysense: A multi-modal remote sensing foundation model towards universal interpretation for earth observation imagery. In: *Proceedings of the IEEE/CVF Conference on Computer Vision and Pattern Recognition*. pp. 27672–27683 (2024)
18. He, K., Sun, J., Tang, X.: Single image haze removal using dark channel prior. *IEEE transactions on pattern analysis and machine intelligence* **33**(12), 2341–2353 (2010)
19. Ho, J., Jain, A., Abbeel, P.: Denoising diffusion probabilistic models. *Advances in neural information processing systems* **33**, 6840–6851 (2020)
20. Huh, M., Cheung, B., Wang, T., Isola, P.: The platonic representation hypothesis. In: *International Conference on Machine Learning* (2024)
21. Jeong, J., Han, S., Kim, J., Kim, S.J.: Latent space super-resolution for higher-resolution image generation with diffusion models. In: *Proceedings of the Computer Vision and Pattern Recognition Conference*. pp. 2355–2365 (2025)
22. Jin, X., He, J., Xiao, Y., Lihe, Z., Liao, X., Li, J., Yuan, Q.: RFE-VCR: Reference-enhanced transformer for remote sensing video cloud removal. *ISPRS Journal of Photogrammetry and Remote Sensing* **214**, 179–192 (2024)
23. Karras, T., Aittala, M., Aila, T., Laine, S.: Elucidating the design space of diffusion-based generative models. *Advances in neural information processing systems* **35**, 26565–26577 (2022)
24. King, M.D., Platnick, S., Menzel, W.P., Ackerman, S.A., Hubanks, P.A.: Spatial and temporal distribution of clouds observed by modis onboard the terra and aqua satellites. *IEEE transactions on geoscience and remote sensing* **51**(7), 3826–3852 (2013)
25. Kingma, D.P., Welling, M.: Auto-encoding variational bayes. *arXiv preprint arXiv:1312.6114* (2013)

26. Li, W., Li, Y., Chan, J.C.W.: Thick cloud removal with optical and SAR imagery via convolutional-mapping-deconvolutional network. *IEEE Transactions on Geoscience and Remote Sensing* **58**(4), 2865–2879 (2019)
27. Li, Z., Shen, H., Weng, Q., Zhang, Y., Dou, P., Zhang, L.: Cloud and cloud shadow detection for optical satellite imagery: Features, algorithms, validation, and prospects. *ISPRS Journal of Photogrammetry and Remote Sensing* **188**, 89–108 (2022)
28. Lipman, Y., Chen, R.T.Q., Ben-Hamu, H., Nickel, M., Le, M.: Flow matching for generative modeling. In: *The Eleventh International Conference on Learning Representations* (2023)
29. Liu, J., Pan, B., Shi, Z.: CR-Famba: A frequency-domain assisted mamba for thin cloud removal in optical remote sensing imagery. *IEEE Transactions on Multimedia* (2025)
30. Liu, X., Gong, C., Liu, Q.: Flow straight and fast: Learning to generate and transfer data with rectified flow. In: *The Eleventh International Conference on Learning Representations* (2023)
31. Liu, Y., Li, W., Guan, J., Zhou, S., Zhang, Y.: Effective cloud removal for remote sensing images by an improved mean-reverting denoising model with elucidated design space. In: *Proceedings of the Computer Vision and Pattern Recognition Conference*. pp. 17851–17861 (2025)
32. Lu, C., Zhou, Y., Bao, F., Chen, J., Li, C., Zhu, J.: DPM-solver: A fast ODE solver for diffusion probabilistic model sampling in around 10 steps. *Advances in neural information processing systems* **35**, 5775–5787 (2022)
33. Luo, Z., Gustafsson, F.K., Zhao, Z., Sjölund, J., Schön, T.B.: Image restoration with mean-reverting stochastic differential equations. *International Conference on Machine Learning* (2023)
34. Ma, N., Goldstein, M., Albergo, M.S., Boffi, N.M., Vanden-Eijnden, E., Xie, S.: SiT: Exploring flow and diffusion-based generative models with scalable interpolant transformers. In: *European Conference on Computer Vision*. pp. 23–40. Springer (2024)
35. Ma, X., Huang, Y., Zhang, X., Pun, M.O., Huang, B.: Cloud-EGAN: Rethinking cycleGAN from a feature enhancement perspective for cloud removal by combining CNN and transformer. *IEEE Journal of Selected Topics in Applied Earth Observations and Remote Sensing* **16**, 4999–5012 (2023)
36. Mehri, A., Ardakani, P.B., Sappa, A.D.: MPRNet: Multi-path residual network for lightweight image super resolution. In: *Proceedings of the IEEE/CVF Winter Conference on Applications of Computer Vision*. pp. 2704–2713 (2021)
37. Nichol, A.Q., Dhariwal, P.: Improved denoising diffusion probabilistic models. In: *International conference on machine learning*. pp. 8162–8171. PMLR (2021)
38. Pan, L., Song, X., Xie, F., Zhang, X., Ji, H., Shi, Z.: M3-CR: Multi-scale multi-branch Mamba for SAR-assisted optical image thick cloud removal. *IEEE Transactions on Geoscience and Remote Sensing* (2025)
39. Peebles, W., Xie, S.: Scalable diffusion models with transformers. In: *Proceedings of the IEEE/CVF international conference on computer vision*. pp. 4195–4205 (2023)
40. Rombach, R., Blattmann, A., Lorenz, D., Esser, P., Ommer, B.: High-resolution image synthesis with latent diffusion models. In: *Proceedings of the IEEE/CVF conference on computer vision and pattern recognition*. pp. 10684–10695 (2022)
41. Silva, L.H.F.P., Mari, J.F., Escarpinati, M.C., Backes, A.R.: Cloud removal with compact diffusion models: A residual block-based approach. *Remote Sensing Applications: Society and Environment* p. 101680 (2025)

42. Siméoni, O., Vo, H.V., Seitzer, M., Baldassarre, F., Oquab, M., Jose, C., Khalidov, V., Szafraniec, M., Yi, S., Ramamonjisoa, M., et al.: DINOv3 (2025)
43. Singh, P., Komodakis, N.: Cloud-Gan: Cloud removal for sentinel-2 imagery using a cyclic consistent generative adversarial networks. In: IGARSS 2018-2018 IEEE International Geoscience and Remote Sensing Symposium. pp. 1772–1775. IEEE (2018)
44. Song, J., Meng, C., Ermon, S.: Denoising diffusion implicit models. arXiv:2010.02502 (October 2020)
45. Song, Y., Sohl-Dickstein, J., Kingma, D.P., Kumar, A., Ermon, S., Poole, B.: Score-based generative modeling through stochastic differential equations. In: International Conference on Learning Representations (2021)
46. Sui, J., Ma, Y., Yang, W., Zhang, X., Pun, M.O., Liu, J.: Diffusion enhancement for cloud removal in ultra-resolution remote sensing imagery. *IEEE Transactions on Geoscience and Remote Sensing* **62**, 1–14 (2024)
47. Wang, C., Guo, L., Fu, Z., Yang, S., Cheng, H., Kot, A.C., Wen, B.: Reconciling stochastic and deterministic strategies for zero-shot image restoration using diffusion model in dual. In: Proceedings of the Computer Vision and Pattern Recognition Conference. pp. 23207–23216 (2025)
48. Wang, Z., Ma, X., Pun, M.O.: Downstream task-aware cloud removal for very-high-resolution remote sensing images: An information loss perspective. *IEEE Journal of Selected Topics in Applied Earth Observations and Remote Sensing* **18**, 24531–24545 (2025)
49. Yang, H., Bulat, A., Hadji, I., Pham, H.X., Zhu, X., Tzimiropoulos, G., Martinez, B.: FAM diffusion: Frequency and attention modulation for high-resolution image generation with stable diffusion. In: Proceedings of the Computer Vision and Pattern Recognition Conference. pp. 2459–2468 (2025)
50. Zamir, S.W., Arora, A., Khan, S., Hayat, M., Khan, F.S., Yang, M.H.: Restormer: Efficient transformer for high-resolution image restoration. In: Proceedings of the IEEE/CVF conference on computer vision and pattern recognition. pp. 5728–5739 (2022)
51. Zhou, S., Chen, D., Pan, J., Shi, J., Yang, J.: Adapt or perish: Adaptive sparse transformer with attentive feature refinement for image restoration. In: Proceedings of the IEEE/CVF Conference on Computer Vision and Pattern Recognition. pp. 2952–2963 (2024)
52. Zhu, Q., Lao, J., Ji, D., Luo, J., Wu, K., Zhang, Y., Ru, L., Wang, J., Chen, J., Yang, M., et al.: Skysense-O: Towards open-world remote sensing interpretation with vision-centric visual-language modeling. In: Proceedings of the Computer Vision and Pattern Recognition Conference. pp. 14733–14744 (2025)
53. Zhu, X.X., Tuia, D., Mou, L., Xia, G.S., Zhang, L., Xu, F., Fraundorfer, F.: Deep learning in remote sensing: A comprehensive review and list of resources. *IEEE geoscience and remote sensing magazine* **5**(4), 8–36 (2017)
54. Zi, Y., Xie, F., Zhang, N., Jiang, Z., Zhu, W., Zhang, H.: Thin cloud removal for multispectral remote sensing images using convolutional neural networks combined with an imaging model. *IEEE Journal of Selected Topics in Applied Earth Observations and Remote Sensing* **14**, 3811–3823 (2021)
55. Zou, X., Li, K., Xing, J., Zhang, Y., Wang, S., Jin, L., Tao, P.: DiffCR: A fast conditional diffusion framework for cloud removal from optical satellite images. *IEEE Transactions on Geoscience and Remote Sensing* **62**, 1–14 (2024)

Supplementary Material

A Proof of the probability flow ODE with the velocity.

In this part, we provide a detailed derivation of the backward process formulation introduced in the main paper. Specifically, we show how the marginal distribution $p_t(x)$ of variable x_t in Eq. (7) satisfies the transport equation and how this leads to the expression of the velocity field $\mathbf{v}_t(x)$ in Eq. (8). Part of proofs are derived from [1].

Consider the time-dependent probability density function $p_t(x)$ of x_t defined in Eq. (4). By definition, its characteristic function $\hat{p}_t(\mathbf{k}) = \int_{\mathbb{R}^d} e^{i\mathbf{k}\cdot x} p_t(x) dx$ is given by:

$$\hat{p}_t(\mathbf{k}) = \mathbb{E}[e^{i\mathbf{k}\cdot x_t}], \quad (16)$$

where \mathbb{E} denotes expectation over x_* , x_c and ϵ . Taking time derivation on both sides, and using the tower property of conditional expectation, we have:

$$\partial_t \hat{p}_t(\mathbf{k}) = i\mathbf{k} \cdot \mathbb{E}[\dot{x}_t e^{i\mathbf{k}\cdot x_t}] \quad (17)$$

$$= i\mathbf{k} \cdot \mathbb{E}_{x \sim p_t}[\mathbb{E}[\dot{x}_t e^{i\mathbf{k}\cdot x_t} \mid x_t = x]] \quad (18)$$

$$= i\mathbf{k} \cdot \mathbb{E}_{x \sim p_t}[\mathbb{E}[(\dot{\alpha}_t x_* + \dot{\beta}_t x_c + \dot{\sigma}_t \epsilon) e^{i\mathbf{k}\cdot x_t} \mid x_t = x]] \quad (19)$$

$$= i\mathbf{k} \cdot \mathbb{E}_{x \sim p_t}[\mathbb{E}[(\dot{\alpha}_t x_* + \dot{\beta}_t x_c + \dot{\sigma}_t \epsilon) \mid x_t = x] e^{i\mathbf{k}\cdot x}] \quad (20)$$

$$= i\mathbf{k} \cdot \mathbb{E}_{x \sim p_t}[\mathbf{v}_t(x) e^{i\mathbf{k}\cdot x}] \quad (21)$$

where $\mathbf{v}_t(x) = \mathbb{E}[(\dot{\alpha}_t x_* + \dot{\beta}_t x_c + \dot{\sigma}_t \epsilon) \mid x_t = x] = \dot{\alpha}_t \mathbb{E}[x_* \mid x_t = x] + \dot{\beta}_t \mathbb{E}[x_c \mid x_t = x] + \dot{\sigma}_t \mathbb{E}[\epsilon \mid x_t = x]$ is the velocity defined in Eq. (8). Furthermore, following Eq. (21), we have:

$$\partial_t \int_{\mathbb{R}^d} e^{i\mathbf{k}\cdot x} p_t(x) dx = i\mathbf{k} \cdot \int_{\mathbb{R}^d} \mathbf{v}_t(x) e^{i\mathbf{k}\cdot x} p_t(x) dx, \quad (22)$$

from which we deduce:

$$\int_{\mathbb{R}^d} e^{i\mathbf{k}\cdot x} \partial_t p_t(x) dx = \int_{\mathbb{R}^d} \mathbf{v}_t(x) \cdot \nabla_x [e^{i\mathbf{k}\cdot x}] p_t(x) dx \quad (23)$$

$$= - \int_{\mathbb{R}^d} \nabla_x \cdot [\mathbf{v}_t(x) p_t(x)] e^{i\mathbf{k}\cdot x} dx, \quad (24)$$

where $\nabla_x \cdot [\mathbf{v} p_t] = \sum_{i=1}^d \frac{\partial}{\partial x_i} [v_i p_t]$ is the divergence operator. By properties of the Fourier transform, this implies that $p_t(\mathbf{x})$ satisfies the transport equation in Eq. (7).

B Downstream Networks

Owing to the strong transferability and generalization capability of DINOv3 across various visual tasks, we adopt the frozen DINOv3 weights as the backbone

of downstream networks. Only lightweight task-specific decoders are trained, as illustrated in Fig. 7. In our implementation, DINOv3 produces both a class token and a set of patch tokens. The class token is used for the CLS task, while the reshaped patch tokens are employed for the three dense prediction tasks, including BLD, SEG, and HE, whose specific designs are described as follows.

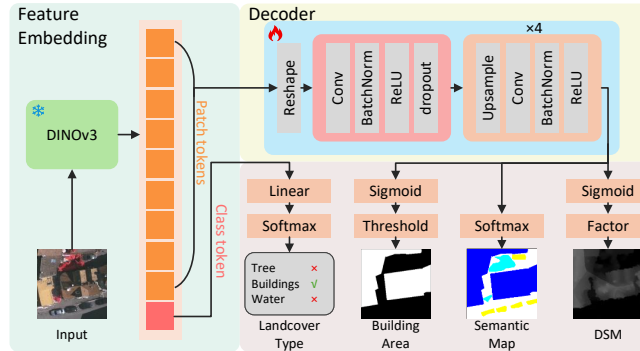


Fig. 7: Downstream Networks.

For the CLS task, we adopt a simple yet effective strategy by directly applying a linear classifier to the class token. The classifier transforms the global representation into category probabilities, which are optimized using the standard cross-entropy loss.

For the three dense prediction tasks, we employ a unified lightweight cascaded decoder to progressively reconstruct spatial resolution from the patch features. Each stage consists of interpolation-based upsampling followed by convolution, activation, and normalization operations, enabling hierarchical refinement of spatial features until the original image scale is restored. A task-specific prediction head is then applied to generate the final output map.

For the BLD task, the prediction head outputs a single-channel probability map, activated by a sigmoid function and optimized using the binary cross-entropy loss. During inference, a fixed threshold of 0.5 is applied to binarize the output into building and non-building regions. For the SEG task, a softmax activation is applied to produce multi-class probability maps, and the network is trained using a pixel-wise cross-entropy loss to ensure accurate semantic labeling. For the HE task, the decoder outputs a normalized height map activated by a sigmoid function, which is optimized using an L1 loss. During evaluation, the predicted normalized heights are rescaled by a constant factor (25.5 in practice) to recover metric height values for quantitative assessment.

C Datasets Details

C.1 CUHKCR-EXT Dataset

The CUHKCR-EXT dataset, introduced by [48], contains 0.5 m ultra-high-resolution images captured by the Jilin-1 satellite. It includes paired cloudy and cloud-free images from two regions in Guangzhou (GZ) and Changsha (CS), China. The CUHKCR-EXT-GZ subset is primarily covered by thin clouds, whereas the CUHKCR-EXT-CS subset exhibits a higher proportion of thick clouds. CUHKCR-EXT consists of two parts: the CR part and downstream tasks part. For the CR subset, CUHKCR-EXT-CS contains 34 large images of size 3000×3000 , and CUHKCR-EXT-GZ includes 31 images of size 3600×3600 . The downstream part provides annotations for six land-cover types based on the LCZ standard [4]. Since the dataset provides unsliced, large-scale images, it enables flexible and customizable alignment for experimental comparison. To support our building extraction task, we manually annotated building regions using the CVAT tool. The annotated regions used for building detection were strictly separated from those used for cloud removal to avoid overlap and ensure independent evaluation. Some samples used for BLD tasks are shown in Fig. 10.

C.2 Synthetic Cloud Dataset

We trained and evaluated our downstream performance based on the ISPRS Vaihingen and ISPRS Potsdam. The Vaihingen and Potsdam datasets are two high-resolution benchmarks widely used for urban scene understanding. The Vaihingen dataset consists of 16 orthophotos (approximately 2500×2000 pixels each) with three spectral bands (near-infrared, red, and green) and a normalized DSM at a ground sampling distance of 9 cm. The Potsdam dataset contains 24 orthophotos of 6000×6000 pixels with four spectral bands (infrared, red, green, and blue) and a DSM at 5 cm resolution; the RGB channels are adopted in our experiments. They share six semantic categories, including building, tree, low vegetation, car, impervious surface, and a background class.

To obtain high-resolution cloudy datasets with SEG and HE annotations, we constructed four cloud removal datasets containing both thin- and thick-cloud types based on the atmospheric scattering model [18] and the cloud generation approach proposed by Czerkawski et al. [8]. To systematically control cloud opacity, we extended the cloud generator with a scalar thickness parameter that jointly scales the mask intensity. To ensure controlled variability, two constraints are imposed: (1) for a fixed thickness, different images exhibit distinct cloud shapes; and (2) within the same image, varying the thickness preserves the overall cloud structure. Sample visualizations are shown in Fig. 11.

D Detailed Experiment Implements

D.1 Training Configurations

To conduct our experiments, we trained GACR for 200k steps with a batch size of 4 and performed validation every 10k steps to select the model with the best

Table 5: Training configurations across datasets.

Dataset	CUHKCR-EXT-GZ	CUHKCR-EXT-CS	Potsdam-CR-thin	Potsdam-CR-thick	Vaihingen-CR-thin	Vaihingen-CR-thick
Training number	3686	2800	3678	3678	1803	1803
Test number	922	700	920	920	451	451
Image size				256 × 256		
Training steps				200k		
Batch size				4		
Precision				tf32		
PERA dim				1024		
Training device	1 × A800	1 × A800	1 × A800	1 × A800	1 × A800	1 × A800
Depth				[2, 2, 2, 2]		
Widths				[128, 256, 512, 1024]		
FPN intermediate widths				[256, 512, 1024, 2048]		
Attention heads				64		
Attention dim				[2, 4, 6, 12]		
Neighborhood kernel size				7		
Dropout rate				[0.0, 0.0, 0.0, 0.1]		
Optimizer				AdamW		
Learning rate				1.0×10^{-4}		
beta ₁				0.9		
beta ₂				0.999		
epsilon				1.0×10^{-8}		
Weight decay				0		
λ				0.5		
Sampling steps				4		

performance. We adopt the AdamW optimizer with $\beta_1 = 0.9$, $\beta_2 = 0.999$, and $\epsilon = 1 \times 10^{-8}$, while the learning rate is set to 1×10^{-4} . Experiments using the DINOv3 ViT-L/16-SAT-300M weights with $p = 1$ are conducted on a single A100 GPU, whereas all other reported results are obtained using a single A800 GPU. All images are resized to 256×256 for both training and inference. Additional training details are summarized in Table 5.

D.2 Compared Methods

We select six representative methods as baselines for comparison. Specifically, MPRNet [36] is a CNN-based method; Restormer [50] and AST [51] are Transformer-based methods; MambaIR [16] is Mamba-based; DFCFormer [48] is dynamic-filter-based; and EMRDM [31] is diffusion-based. Although the PSNR and SSIM results of MPRNet, Restormer, AST, MambaIR, and DFCFormer were reported in [48], we retrain all these models to ensure fair comparison, since our experiments re-slice the original images to construct training sets that do not overlap with the BLD task. EMRDM is trained for 400k steps following its original configuration, while the other methods are trained for 100 epochs using their default settings. All reported results correspond to the checkpoints achieving the best validation performance.

D.3 Evaluation Metrics

Cloud Removal (CR). For the CR task, we evaluate the image restoration quality using four widely used metrics: Peak Signal-to-Noise Ratio (PSNR), Structural Similarity Index (SSIM), Learned Perceptual Image Patch Similarity (LPIPS), and Root Mean Squared Error (RMSE). The PSNR measures the reconstruction

fidelity between the restored image \hat{I} and the ground-truth clear image I , defined as:

$$\text{PSNR} = 10 \log_{10} \left(\frac{L^2}{\frac{1}{N} \sum_{i=1}^N (I_i - \hat{I}_i)^2} \right), \quad (25)$$

where L is the maximum possible pixel value (e.g., 255 for 8-bit images), and N denotes the total number of pixels. The SSIM measures the structural similarity between two images, formulated as:

$$\text{SSIM}(I, \hat{I}) = \frac{(2\mu_I \mu_{\hat{I}} + C_1)(2\sigma_{I\hat{I}} + C_2)}{(\mu_I^2 + \mu_{\hat{I}}^2 + C_1)(\sigma_I^2 + \sigma_{\hat{I}}^2 + C_2)}, \quad (26)$$

where μ and σ denote mean and standard deviation, $\sigma_{I\hat{I}}$ represents cross-covariance, and C_1, C_2 are small constants to stabilize the division.

LPIPS measures the perceptual distance between two images based on deep feature representations extracted by pretrained networks, and smaller LPIPS values indicate better perceptual quality, which is defined as:

$$\text{LPIPS}(I, \hat{I}) = \sum_l \frac{1}{H_l W_l} \sum_{h=1}^{H_l} \sum_{w=1}^{W_l} \left\| w_l \odot (\phi_l(I)_{hw} - \phi_l(\hat{I})_{hw}) \right\|_2^2, \quad (27)$$

where $\phi_l(\cdot)$ denotes the feature map of layer l from the pretrained network, H_l and W_l are its spatial dimensions, w_l is a learned weight vector that calibrates channel-wise importance, and \odot represents element-wise multiplication.

The RMSE quantifies pixel-wise error:

$$\text{RMSE} = \sqrt{\frac{1}{N} \sum_{i=1}^N (I_i - \hat{I}_i)^2}. \quad (28)$$

Classification (CLS). For the classification task, the overall accuracy (Acc) is used to evaluate model performance:

$$\text{Acc} = \frac{N_{\text{correct}}}{N_{\text{total}}}, \quad (29)$$

where N_{correct} is the number of correctly classified samples and N_{total} is the total number of samples.

Building Detection (BLD). For the building detection task, the Intersection over Union (IoU) is adopted to measure the overlap between predicted and ground-truth building masks:

$$\text{IoU} = \frac{|P \cap G|}{|P \cup G|}, \quad (30)$$

where P and G represent the predicted and ground-truth building regions, respectively. A higher IoU indicates better localization consistency.

Table 6: Comparison of model complexity in terms of FLOPs and parameters.

Model	MPRNet	Restormer	AST	MambaIR	DFCFormer	EMRDM	GACR/2	GACR/1
FLOPs (G)	548.65	140.99	38.86	206.80	138.45	166.72	56.05	223.60
Params (M)	3.64	26.10	19.90	3.16	29.98	39.13	73.81	73.80

Semantic Segmentation (SEG). For semantic segmentation, the mean Intersection over Union (mIoU) is used to evaluate the overall multi-class segmentation accuracy:

$$\text{mIoU} = \frac{1}{C} \sum_{c=1}^C \frac{|P_c \cap G_c|}{|P_c \cup G_c|}, \quad (31)$$

where C is the number of semantic classes, and P_c and G_c denote the predicted and ground-truth regions for class c .

Height Estimation (HE). For the height estimation task, the Root Mean Squared Error (RMSE) is employed to measure the deviation between the predicted and reference DSMs:

$$\text{RMSE} = \sqrt{\frac{1}{N} \sum_{i=1}^N (H_i - \hat{H}_i)^2}, \quad (32)$$

where H_i and \hat{H}_i are the ground-truth and predicted height values for pixel i , respectively, and N is the total number of valid pixels.

E Additional Experiments

E.1 Model Complexity

As shown in Table 6, the GACR model with $p = 2$ achieves a favorable trade-off between efficiency and capacity, requiring only 56.05G FLOPs while maintaining competitive performance among all compared methods. This compact configuration highlights the efficiency advantage of the proposed design. Although the $p = 1$ variant can further improve the visual quality of cloud removal results, as reported in Tab. 1, it introduces a substantial increase in computational cost (223.60G FLOPs). Therefore, we primarily adopt the $p = 2$ configuration for comparison in subsequent experiments to maintain a balanced evaluation between effectiveness and efficiency.

E.2 Visualization of t-SNE

We perform t-SNE visualization to analyze how CR influences the CLS task. Class tokens extracted from CUHKCR-EXT-GZ using the DINOv3 ViT-L/16-SAT-300M weights are projected into a t-SNE space fitted on clear-image features, as shown in Fig. 8. The results show that even without CR, cloudy images

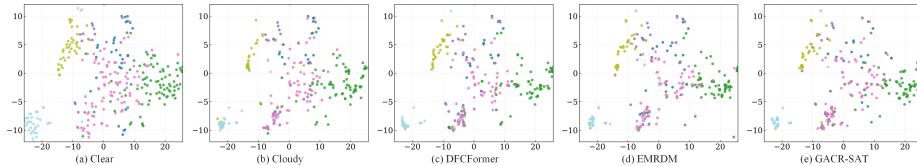


Fig. 8: The t-SNE visualization of feature representations on the CUHKCR-EXT-GZ dataset using the DINOv3 ViT-L/16-SAT-300M weights.

Table 7: Quantitative comparison of downstream performance on ViT-L/16-SAT-300M weight across four downstream tasks, including classification (CLS), building extraction (BLD), semantic segmentation (SEG), and height estimation (HE). The best and second-best results are highlighted in **bold** and underline, respectively.

Model	CLS-1 Acc. \uparrow	CLS-2 Acc. \uparrow	BLD-1 IoU \uparrow	BLD-2 IoU \uparrow	SEG-1 mIoU \uparrow	SEG-2 mIoU \uparrow	SEG-3 mIoU \uparrow	SEG-4 mIoU \uparrow	HE-1 RMSE \downarrow	HE-2 RMSE \downarrow	HE-3 RMSE \downarrow	HE-4 RMSE \downarrow
Upper Bound	0.882	0.896	0.726	0.773	0.731	0.731	0.742	0.742	2.001	2.001	1.570	1.570
Lower Bound	0.686	0.454	0.607	0.497	0.449	0.334	0.554	0.378	2.737	3.489	2.272	2.949
End-to-End	0.830	0.890	0.694	0.709	0.686	0.593	0.706	0.623	2.217	2.622	1.715	2.050
MPRNet	0.498	0.500	0.654	0.534	0.677	0.559	0.675	0.569	2.280	2.905	1.711	2.078
Restormer	0.542	0.533	0.664	0.572	0.690	0.591	0.677	0.600	2.166	2.540	1.628	1.889
AST	0.415	0.435	0.673	0.620	0.636	0.469	0.629	0.490	2.449	3.143	1.799	2.406
MambaIR	0.458	0.484	0.667	0.501	0.682	0.547	0.659	0.602	2.241	2.910	1.688	1.921
DFCFormer	0.639	0.500	0.667	0.555	0.681	0.574	0.663	0.621	2.225	2.679	1.656	1.876
EMRDM	0.642	0.647	<u>0.699</u>	0.681	0.709	0.641	<u>0.730</u>	0.634	2.092	2.353	1.599	1.830
GACR-SAT	<u>0.753</u>	<u>0.729</u>	0.700	0.707	0.727	0.676	0.740	<u>0.692</u>	2.061	<u>2.236</u>	1.582	1.682
GACR-LVD	0.833	0.742	0.697	<u>0.702</u>	<u>0.715</u>	<u>0.673</u>	0.727	0.698	<u>2.062</u>	2.229	<u>1.589</u>	<u>1.682</u>

already form well-separated clusters corresponding to different classes. Applying various CR methods does not further improve the separability between clusters. This phenomenon likely arises because classification primarily relies on global representations, which are only weakly affected by localized cloud noise. Consequently, the end-to-end approach can achieve performance comparable to, or even better than, most CR-based preprocessing pipelines.

E.3 Downstream performance with DINOv3-SAT backbone

In Tab. 2, we report the results obtained using ViT-L/16-LVD-1689M as the pre-trained backbone for downstream networks. We further evaluate the performance using the ViT-L/16-SAT-300M weights. As shown in Tab. 7, GACR consistently outperforms other methods under this downstream setting, further demonstrating the effectiveness of the proposed framework. Notably, we observe that most models exhibit a certain degree of performance degradation when switching from LVD to SAT weights, which may be attributed to the richer and more diverse pretraining data used by LVD.

These results provide a practical insight into the use of different DINOv3 weights for remote sensing tasks. The SAT weights, pretrained on remote sensing datasets, capture more domain-specific representations that benefit low-level

Table 8: Quantitative comparison of SEG tasks with A^2 -FPN (ResNet-based) and UNetFormer (CNN-Transformer Hybrid).

Method	Vaihingen-CR-thin		Vaihingen-CR-thick	
	A^2 -FPN	UNetFormer	A^2 -FPN	UNetFormer
Upper Bound	0.747	0.687	0.747	0.687
Lower Bound	0.384	0.289	0.277	0.231
MPRNet	0.713	0.623	0.619	0.527
Restormer	0.731	0.653	0.687	0.599
AST	0.718	0.622	0.587	0.513
MambaIR	0.725	0.642	0.668	0.566
DFCFormer	0.728	0.645	0.695	0.617
EMRDM	0.731	0.655	0.688	0.584
GACR-SAT/2	0.739	0.678	0.721	0.662
GACR-LVD/2	<u>0.739</u>	<u>0.677</u>	<u>0.719</u>	<u>0.653</u>

tasks such as image restoration. In contrast, the LVD weights, pretrained on a broader and more diverse corpus, offer stronger semantic understanding capabilities and are therefore more suitable for high-level downstream tasks. Additionally, differences in the input resolution used during pretraining may also contribute to the observed domain discrepancy between the two pretrained models.

E.4 Evaluation on Heterogeneous Downstream Architectures.

To further examine the robustness of the proposed framework with respect to downstream model architectures, we conduct additional experiments using two heterogeneous segmentation networks: the ResNet-based A^2 -FPN and the CNN-Transformer hybrid UNetFormer. Both networks are trained on cloud-free data following the same evaluation protocol described in the main text. The quantitative results on the Vaihingen-CR dataset are summarized in Table R1.

As shown in Tab. 8, GACR consistently achieves the best or second-best performance across all configurations. On the Vaihingen-CR-thin setting, GACR-SAT obtains mIoU scores of 0.739 and 0.678 when evaluated with A^2 -FPN and UNetFormer, respectively. Similar improvements are observed under the more challenging Vaihingen-CR-thick condition, where GACR-SAT reaches 0.721 and 0.662. These results demonstrate that the performance gains brought by GACR are not tied to a specific downstream backbone but remain effective across heterogeneous architectures.

This behavior suggests that the proposed geo-contextual alignment helps restore semantically meaningful structures that are beneficial for recognition, enabling consistent improvements across different downstream models.

Table 9: Comparison of CKNNA between CR images and cloud-free references across six datasets.

Method	CUHKCR-EXT-GZ	CUHKCR-EXT-CS	Potsdam-CR-thin	Potsdam-CR-thick	Vaihingen-CR-thin	Vaihingen-CR-thick
cloudy	0.319	0.330	0.472	0.584	0.592	0.477
MPRNet	0.328	0.362	0.641	0.535	0.661	0.566
Restormer	0.338	0.371	0.666	0.564	0.699	0.596
AST	0.334	0.363	0.618	0.506	0.628	0.521
MambaIR	0.328	0.362	0.654	0.538	0.679	0.588
DFCFormer	0.338	0.373	0.657	0.553	0.689	0.598
EMRDM	0.346	0.379	0.700	0.592	0.727	0.613
GACR-SAT	0.352	0.388	0.710	0.616	0.747	0.665
GACR-LVD	<u>0.347</u>	<u>0.386</u>	<u>0.706</u>	<u>0.610</u>	<u>0.739</u>	<u>0.657</u>

E.5 CKNNA with Cloud-free Data

To provide a more intuitive comparison of the representational consistency between CR images and their cloud-free counterparts, we compute the CKNNA [20] scores between each CR result and its corresponding cloud-free reference for all competing methods. As shown in Table 9, the CKNNA values of most CR results are generally higher than those of the original cloudy images, indicating improved feature-level alignment after cloud removal. Notably, on the Potsdam-CR-thick dataset, some methods yield slightly lower CKNNA scores than the cloudy images, suggesting that their reconstructed results deviate more from the cloud-free representations. In contrast, GACR achieves consistently higher CKNNA scores across most datasets, demonstrating its stronger capability to enhance representation consistency between the restored and cloud-free images.

E.6 Additional Visual Results

In this section, we present additional visualization results. Fig. 9 illustrates the detailed forward and reverse processes of OAR-Flow. Fig. 12, Fig. 13, Fig. 14, and Fig. 15 provide additional visual comparisons on the CUHKCR-EXT-GZ, CUHKCR-EXT-CS, Potsdam-CR-thick, and Vaihingen-CR-thick datasets, respectively.

E.7 Additional Ablation Studies

Effect of VFM backbones. To examine whether the effectiveness of GCPA depends on a specific visual foundation model, we replace the DINOv3 encoder with DINOv2, CLIP, and MAE while keeping OAR-Flow unchanged. As shown in Tab. 10, all VFM variants consistently outperform the baseline, indicating that the improvement is not tied to a particular encoder choice. DINOv3 achieves the best overall performance, while DINOv2 and CLIP also provide clear gains, confirming the generality of using semantic priors for cloud removal.

Effect of the anchoring strength ρ . We further study the influence of the observation anchoring strength ρ in OAR-Flow. As shown in Tab. 11, increasing ρ from 0 to 3 improves the reconstruction quality, with PSNR increasing from

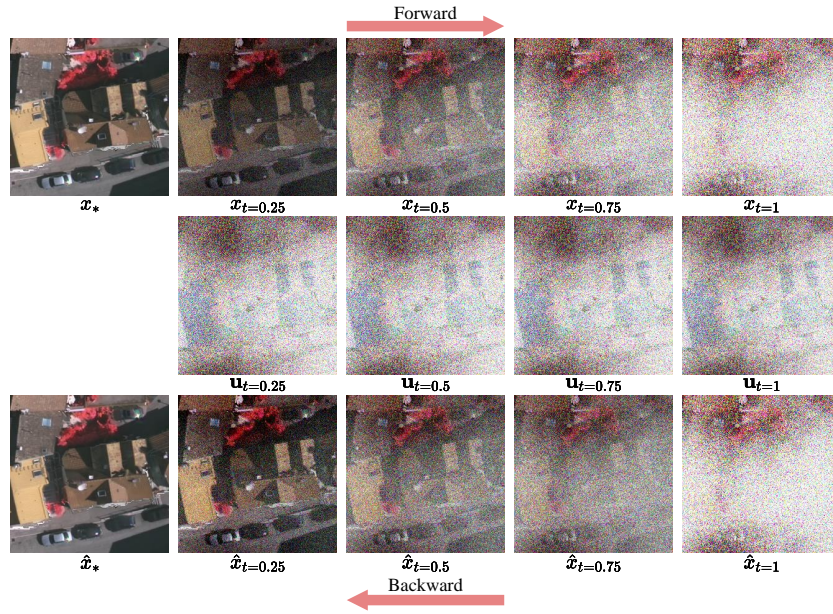


Fig. 9: Visualization of the forward and reverse processes of the OAR-Flow model.

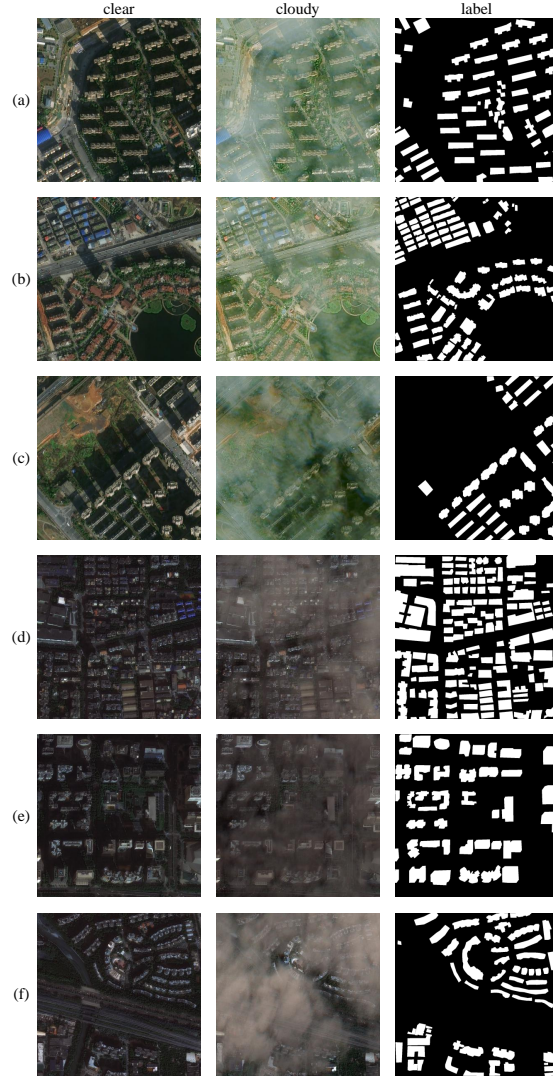
Table 10: Ablation study of different VFM backbones on Vaihingen-CR-thick.

Backbone	PSNR \uparrow	SSIM \uparrow	SEG \uparrow	HE \downarrow
DINOv2	32.552	0.962	0.726	1.564
CLIP	32.203	0.962	0.725	1.566
MAE	31.096	0.955	0.720	1.606
Baseline	28.979	0.951	0.692	1.629

32.264 to 33.018. This suggests that moderate anchoring helps preserve reliable observation cues and stabilizes the reverse trajectory. When ρ is further increased, the performance slightly drops, indicating that overly strong anchoring may restrict the model’s ability to recover heavily obscured regions. We therefore adopt $\rho = 3$ by default.

Table 11: Ablation study of the anchoring strength ρ on Vaihingon-CR-thick.

ρ	0	1	2	3	4	5
PSNR \uparrow	32.264	32.648	33.006	33.018	32.876	32.672

**Fig. 10:** Sample visualization for the BLD task. From left to right are the clear image, cloudy image, and building area label. Panels (a-c) are selected from the CUHKCR-EXT-CS dataset, while panels (d-f) are taken from the CUHKCR-EXT-GZ dataset.

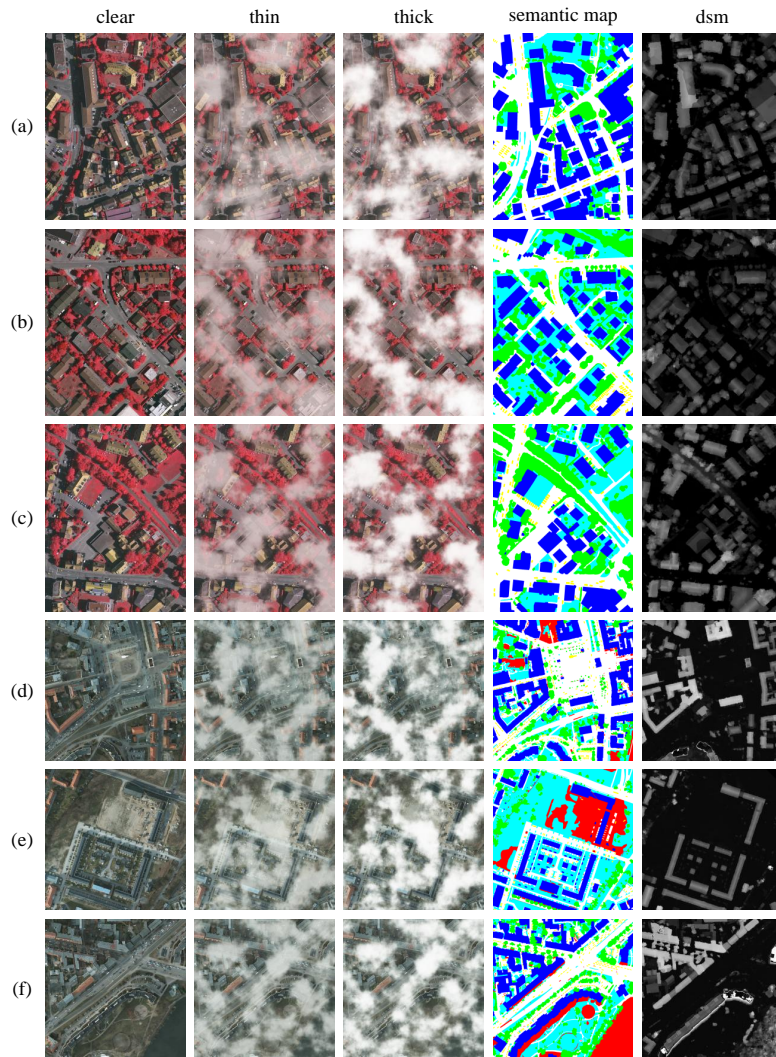


Fig. 11: Sample visualization for the SEG and HE tasks. From left to right are the clear image, thin-cloud image, thick-cloud image, semantic map, and DSM. Panels (a-c) are selected from the Vaihingen-CR-thin and Vaihingen-CR-thick datasets, while panels (d-f) are taken from the Vaihingen-CR-thick dataset.

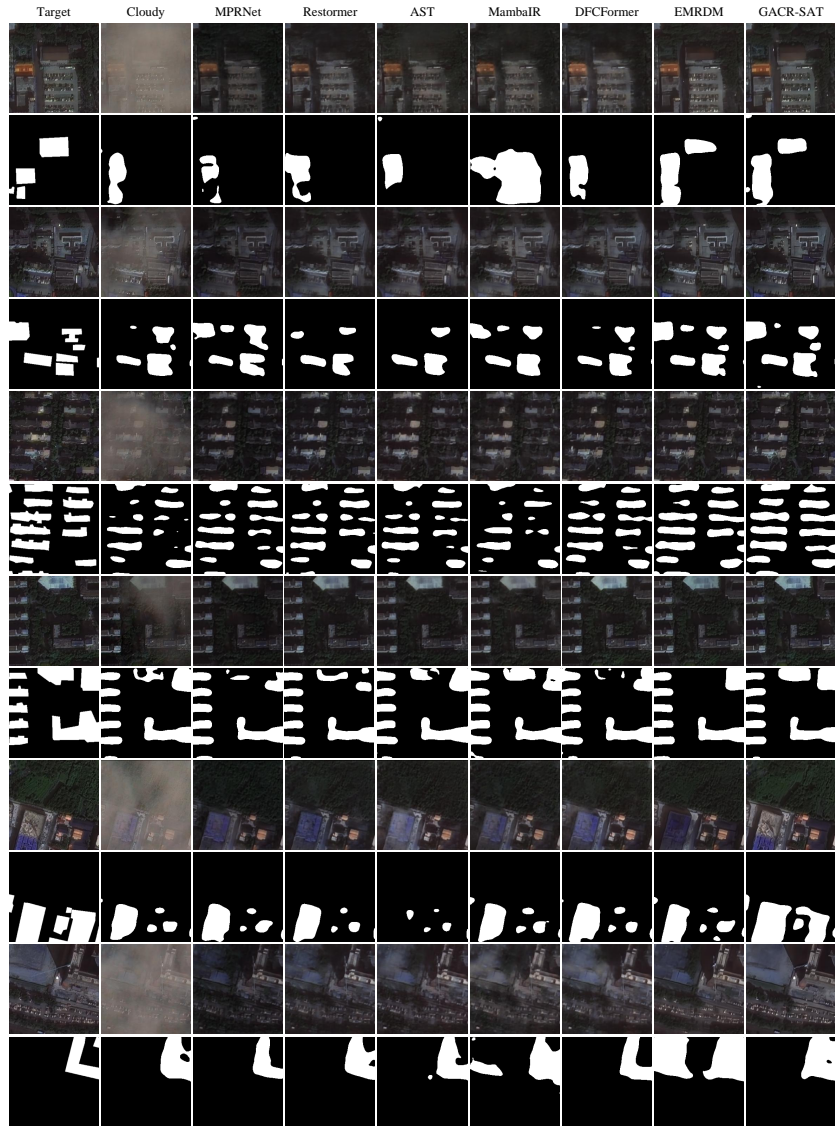


Fig. 12: Additional CR results on CUHKCR-EXT-GZ and the corresponding BLD results.



Fig. 13: Additional CR results on CUHKCR-EXT-CS and the corresponding BLD results.

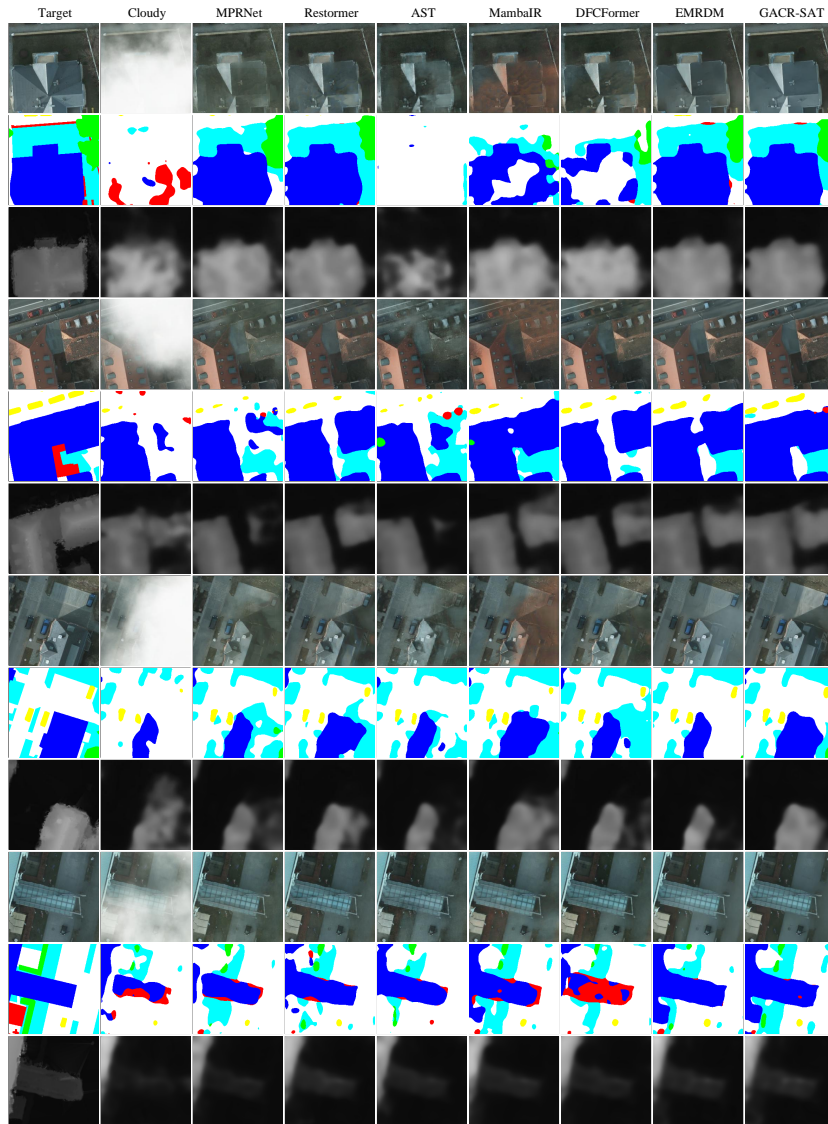


Fig. 14: Additional CR results on Potsdam-CR-thick and the corresponding SEG and HE results.

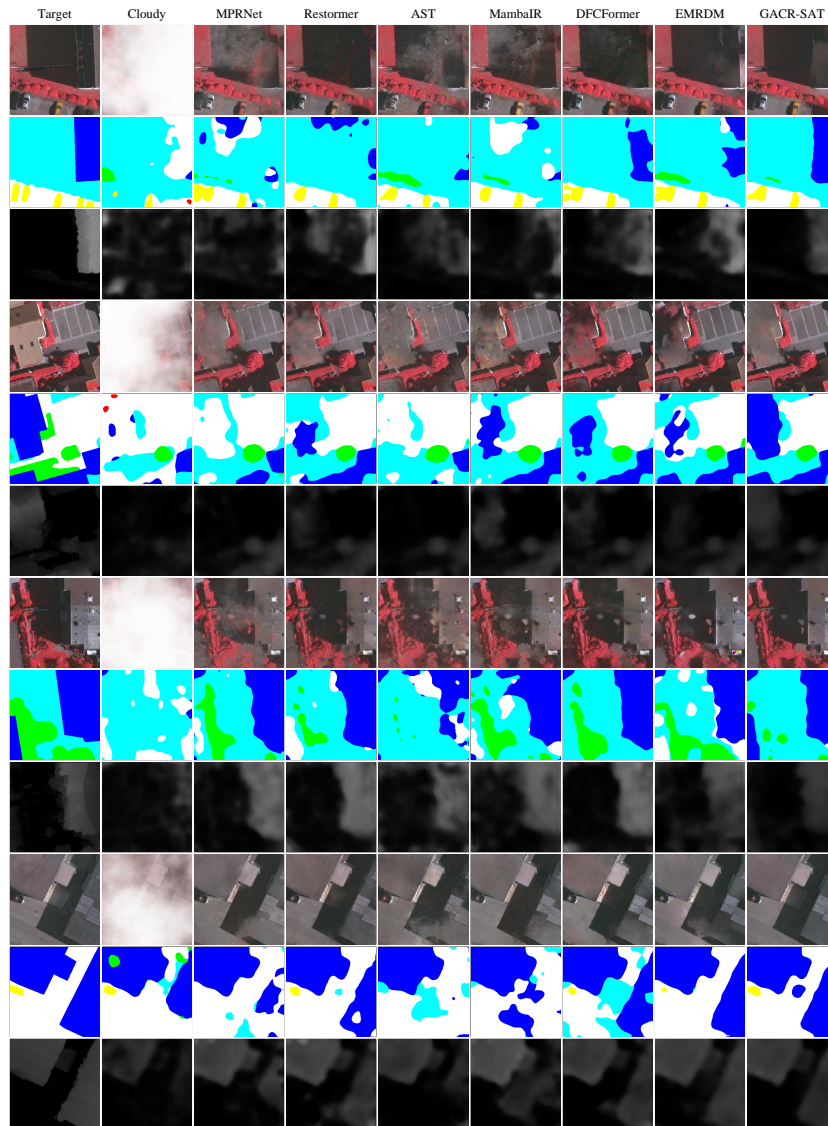


Fig. 15: Additional CR results on Vaihingen-CR-thick and the corresponding SEG and HE results.